SOURCE CHARACTERIZATION OF MICROEARTHQUAKES INDUCED BY HYDRAULIC FRACTURING WITH EMPIRICAL GREEN'S FUNCTION

Yingping Li, C. H. Cheng, and M. Nafi Toksöz

Earth Resources Laboratory
Department of Earth, Atmospheric, and Planetary Sciences
Massachusetts Institute of Technology
Cambridge, MA 02139

ABSTRACT

In this paper, we retrieved relative source time functions (RSTF) and estimated the source parameters for microearthquakes (M= -1.9 to -2.6) induced by hydraulic injection at Fenton Hill, New Mexico, using an empirical Green's function (EGF) method. Seismic waveform of a small event in seismic doublets or multiplets (Gelle and Meuller, 1980), defined as co-located events with similar focal mechanisms, within a hydraulic fracture zone, is treated as the EGF and is deconvolved from that of a larger event in the doublets or multiplets to retrieve the relative source time function. Time domain analysis of the RSTFs reveals the source complexity of the induced microearthquakes. The azimuthal variation of the RSTF indicates that the rupture propagates to the northwest, which is consistent with the growth direction of the hydraulic fracture zone determined by Li and Cheng (1995) with a seismicity temporal-spatial distribution pattern. The source duration of the induced events ranges from 2 to 8 ms and the source radii are estimated to be 4 to 12 meters. Values of stress drops are from 1 to 19 bars. Significant variation of the stress drops may reflect the heterogeneity of the stress field in the hydraulic fracture zone and its vicinity and indicate that the stress field heterogeneity extends down to a few meters.

INTRODUCTION

The source time function (STF) of a seismic event reflects the time history of the rupture process and contains important parameters which characterize physical properties

of the seismic source. However, an observed seismogram is not only a record of ground motion, but also includes the effects of earth structure and instrument response. Therefore, retrieval of a STF from the observed seismograms requires isolating the effects of the propagation path, and recording site and instrument response. That is, the Green's function between the source and receivers must be deconvolved from the data or accounted for in an inversion of the data. This has been traditionally accomplished using the theoretical Green's function (TGF) computed for a reference earth model, either by direct deconvolution or by waveform modeling. A major problem of the TGF methods is that they require detailed knowledge of the Earth's structure and attenuation effects.

An alternative approach to remove the responses of the Earth's structure and the seismic instrument from the observed seismogram is the use of the empirical Green's function (EGF) deconvolution method (e.g., Mueller, 1985; Frankel *et al.*, 1986; Li and Thurber, 1988). The principal idea behind the EGF method is as follows: If two seismic events have much the same hypocental location and a similar focal mechanism but different sizes (e.g., two nearby explosions, or an earthquake and one of its foreshocks and aftershocks), and if the smaller event has a short enough duration and a smaller enough source dimension to be considered impulsive in both time and space domain, then one can treat the waveform of the smaller event as EGF (Hartzell, 1978) and deconvolve it from that of the larger event to obtain a relative STF (Mueller, 1985). This follows from the fact that the pair of two events shares almost the same propagation path to a given receiver and is recorded by the identical instrument. Therefore, the deconvolution of waveforms of the larger event with those of the smaller event removes the path propagation effects, as well as the local receiver site and instrument response, with high accuracy and efficiency.

The EGF method has been successfully applied to retrieve the STF and estimate the source parameters for microearthquakes and large earthquakes, using local seismic network data (e.g., Mueller, 1985; Frankel *et al.*, 1986; Li and Thurber, 1988; Hutchings and Wu, 1990; Mori and Frankel, 1990; Li *et al.*, 1995a, and many others), strong motion data (Hartzell, 1978; Chen *et al.*, 1991; Kanamori *et al.*, 1992), and regional and teleseismic data (Hartzell, 1989, Ammon *et al.*, 1993, Li and Toksöz, 1993; Velasco *et al.*, 1994; Lay *et al.*, 1994; Li *et al.*, 1995b,c). This technique has also been used to study the source mechanism of volcano eruption in Mount St. Helens (Burger and Langston, 1985) and to characterize seismic sources of mining tremors (Li *et al.*, 1994) and nuclear explosions (Li *et al.*, 1995b). However, to the best of our knowledge, few studies have been done with the EGF approach to retrieve the STF of microearthquakes induced by hydraulic fracturing.

Spectral analysis techniques have been used in previous studies of source parameters of the induced microearthquakes by hydraulic fracturing (e.g., Pearson, 1982; Fehler and Phillips, 1991). To obtain reliable estimates of the source parameters, Fehler and Phillips (1991) developed an inversion method for simultaneously inverting for Q and source parameters. By determining the source radii of the induced microearthquakes, they can obtain an estimate of the area of the fractured surface over which fluid may flow in a

fractured reservoir. In this paper, we use the EGF method to retrieve the relative source time functions (RSTF) for 16 larger microearthquakes induced by hydraulic fracturing and estimate the source parameters of these seismic events by the time domain analysis of the RSTFs. The great advantage of this EGF approach is that detailed knowledge about the Earth's structure and attenuation is not required.

DATA AND METHOD

Waveform Data

Seismic waveform data used in this study were collected during a hydraulic fracturing experiment conducted in December 1983 at the Los Alamos Hot Dry Rock (HDR) geothermal test site located at Fenton Hill, New Mexico. During experiment 2032, approximately 21 600 m^3 of water was injected into a wellbore at a depth of 3460 m below the surface. During 61 hours of the water injection experiment, more than 10,000 locatable microearthquakes induced by hydraulic fracturing were recorded by four borehole seismic stations, EE1, EE3, GT1, and PC1 (House, 1987). Stations EE1 and EE3 were equipped with triaxial geophones but stations GT1 and PC1 only had vertical component seismometers. Seismic waveform data were recorded in an analog tape recorder and later digitized at a sampling rate of 5000 samples per second (Fehler and Phillips, 1991).

Seismic waveform data for a small subset of the induced microearthquakes (about 176) recorded during experiment 2032 were obtained from scientists of the Los Alamos National Laboratory. Using the waveform correlation analysis technique and a grid search location algorithm, Li and Cheng (1995, this issue) have determined precise hypocenter locations for 157 induced microearthquakes which occurred during 08:00 to 20:00, December 7, 1983. Among the 157 earthquakes, 147 events define a tight cluster with dimension of order of 40 meters (Figure 1). The cluster delineates an approximate vertical hydraulic fracture zone striking in the northwest-southeast direction. The height and length of the fracture zone are measured about 35 and 40 meters, respectively. Analyzing the spatial-temporal variation of the induced seismicity, Li and Cheng (1995, this issue) found that the length of the hydraulic fracture zone grew rapidly during 09:00 to 11:00, December 7, 1983. The fracture zone grows dominantely toward the northwest along a strike of $N40°W$, with a growth rate of 0.1 to 0.2 meters per minute.

Since the 147 event are concentrated in a tight cluster, it is possible to find suitable seismic doublets for the EGF analysis. We have selected 16 larger events with magnitudes of -1.9 to -2.6 as the main events (Table 1) and will use the EGF method to retrieve the STFs of the main events. The magnitudes in Table 1 are estimated with the maximum amplitudes of S waves and coda lengths (Pearson, 1982). Figure 2 plots the temporal distribution of these 16 main events. It is clearly shown that the majority of the main events occurred during a two hour period from 09:00 to 11:00, December 7, 1983, consistent with the temporal-spatial distribution pattern of smaller earthquakes which occurred within the hydraulic fracture zone defined by the tight clus-

Table 1: Hypocenter Parameters of 16 Main Microearthquakes

Event	Nx(m)	Ey(m)	Dz(m)	EE1(A)	GT1(A)	Mag.
2727	-482	-294	-3295	3345*	2231	-2.0
2732	-486	-292	-3293	1894	1157	-2.5
2774	-482	-294	-3296	3074	1344	-2.2
2880	-491	-292	-3286	1526	449	-2.6
2940	-496	-278	-3287	2800	872	-2.3
2967	-492	-284	-3280	3135	1499	-2.2
2994	-495	-278	-3288	1590	556	-2.5
3023	-483	-292	-3298	3349*	2091	-2.0
3035	-489	-289	-3282	1585	844	-2.4
3041	-490	-284	-3280	2449	1551	-2.2
3095	-496	-278	-3289	3257	1290	-2.2
3130	-492	-284	-3283	2184	970	-2.3
3166	-501	-272	-3281	3336	2014	-2.1
3280	-481	-296	-3299	3365*	2796	-1.9
3600	-480	-296	-3295	3346*	2804	-1.9
3722	-502	-272	-3278	1966	1500	-2.3

ter. Hypocentral locations of 16 main events with magnitudes of -1.9 to -2.6 are shown by three orthogonal views in Figure 3. These 16 main events are well-distributed in the hydraulic fracturing zone and we can infer the mechanical properties of the fracture zone by analyzing the source parameters of these larger microearthquakes.

Searching the location catalog, we can find one or more EGF events for each of the main events. The hypocenter differences between a main event and its EGF counterparts are typically less than 5 meters. The amplitudes of the main events are typically larger than those of the EGF events by factors of 5 to 10, corresponding to magnitudes of 0.7 to 1.0 smaller than those of the main events. It is difficult to well-constrain focal mechanisms with data from a few stations, but we check the polarities of a main event and the EGF events to ensure that they have similar focal mechanisms. The geometry of three borehole stations are also shown in Figure 3 along with the cluster of 16 main events. Waveforms of main events recorded at station EE3 are clipped and the clipped data are excluded from this study. Among 16 main events, 12 were well-recorded on scales at station EE1. Because station EE1 is relatively close to the cluster, signal to noise is very good for both main events and EGF events. Therefore, this station will be a key station in retrieving the STFs for main events. Unfortunately, the four largest main events (2727, 3023, 3280, and 3600 marked with stars in Table 1) are clipped at station EE1, and we have to use waveforms recorded at station GT1 to extract the STFs for the four largest microearthquakes. The site condition of station PC1 is relatively poor and the signal to noise ratio for smaller events is even worse. It is relatively difficult to select very small EGF events. Due to this limitation, we only derive the STF for

event 2967 with data recorded by all three stations. The STFs of other main events are retrieved from only one station, either EE1 or GT1.

Empirical Green's Function Method

Figure 4 illustrates the EGF deconvolution method with an example. The top frame of Figure 4 is a vertical component seismogram recorded at station EE1 for event 2732. We note that a small foreshock (2732f) occurred about 0.15 s before the main event. In the middle frame of Figure 4, we align seismograms of the two events (2732 and 2732f) by the first P wave arrivals and find that the two waveforms are very similar, polarities of the first P wave are the same, and the differential times (S-P) for the two event are almost identical. The maximum amplitude of the larger event is about eight times larger than that of the foreshock. Therefore, the smaller foreshock is a suitable EGF event. The P and S waveforms of the smaller event were used as the EGF and deconvolved from those of the larger event to obtain the relative STF for the larger event (Figure 4, bottom frame). After deconvolution, a fourth-order Butterworth low-pass filter with a corner frequency of 1200 Hz was used to reduce the high frequency noise. The time windows we used for P and S waves are 0.05 and 0.12 s, respectively. The time shift between the peaks of the STFs retrieved with P and S waves is only 0.6 ms, indicating that the hypocentral locations of the two events are very close to each other.

We also tried to retrieve the RSTF of the main event with multiple EGF events. Figure 5 shows the STF of a main event (3095) retrieved with 10 different EGF events using both P and S waves recorded at station EE1. The separations between the peaks of STFs obtained by P and S waves are within 1 to 2 ms, indicating the events we selected as EGF events are indeed very close to the main event. The peak amplitude variations of the RSFTs reflect the slight differences among the sizes of the EGF events, while the slight variation of the RSTF pulse widths indicates that the source durations of the EGF events are not identical. These variations provide some ideas about the error bars of the estimated RSTFs. The bottom two traces are stacked RSTFs for both P and S waves, which present averaged RSTFs. Since we did not align them by the pulse peaks, these stacked results may overestimate the pulse width of the real STF. We also stack the RSTFs obtained with P and S waves of multiple EGF events by aligning them with the pulse peaks and show them in Figure 6. Both P and S wave stacked RSTF traces are sharper than those shown at the bottom of Figure 5. We believe that the averaged RSTFs well-approximate the true STF. The pulse width of event 3095 is measured to be about 2.5 ms. It is also clearly shown that the S wave results are better than those derived from P waves because the signal to noise ratio is better for the S waves.

Retrieving RSTF with the EFG method can also reveal the complex rupture process of an induced microearthquake. The RSTFs of event 2774 in Figure 7 indicate the earthquake is a complex event with two major subevents separated by about 12 ms. A smaller event can be barely seen on the RSTFs extracted with S waves but not on the P wave traces, probably due to the low signal to noise ratio of P waves. Nevertheless,

both P and S wave results indicate that the event is a complex event consisting of multiple episodes of rupture. We stack the STFs retrieved with P and S waves (Figure 8) separately to obtain a better estimation of the source duration for each subevent. The source durations of two major subevents are estimated about 4.5 and 2 ms, respectively. Since S waves have relatively larger signal to noise ratio and result in a better RSTF, we will use mainly S waves to retrieve RSTFs and characterize source properties.

RESULTS AND DISCUSSION

Source Duration, Radius, and Stress Drop

Using the EGF method and S waveform data recorded at station EE1, we have retrieved RSTFs for 12 main events and shown the results in Figure 9. We found that some of the STFs are simple pulses but others have multiple pulses, reflecting a complex rupture process for small events with magnitudes less than -2. The top frame of Figure 10 shows vertical component seismograms of the four largest events (2727, 3280, 3600, 3023) recorded at station GT1 and a close by smaller event 2583, whose S waveform we will use as the EGF. The maximum amplitude of the smaller event is about 5 to 12 times smaller than the four main events. We also see that the signal to noise ratio for the P wave of the EGF event is relatively poor. Therefore, we use only S waves to retrieve the RSTFs of the four main events (bottom frame of Figure 10). Among the four largest events (M = -1.9 to -2.0), three of them are simple pulse, but (3023) appears to be a double event. A smaller microearthquake precedes a larger event by about 57 ms. Figure 11 shows the RSTFs of event 2727 extracted with three different EGF events. These results are very similar to each other and indicate that we can obtain a reliable estimate of the RSTF no matter which EGF events we use. The slight differences among the pulse widths provide some information about error bars of the estimates of RSTF durations.

We measure the source durations (T) and rise time (t1/2) from the RSTFs of 16 main events shown in Figures 9 and 10 and list them in Table 2. The source durations of these events range from 2.2 to 7.6 ms. The source radii are calculated with both rise times (Boatwright, 1980) and source durations (Fukao and Kikuchi, 1987), assuming the rupture velocity is 0.8 Vs. An average radius for each event is shown in Table 2. The source radii are estimated from 3.5 to 12 meters. Using an empirical relationship between the coda magnitude and the seismic moment derived by Pearson (1982), we calculate the seismic moments from the 16 main events and find that the seismic moments are from 1.6×10^15 to 5.4×10^15 dyn-cm. The static stress drops (Brune, 1970) are calculated for the 16 main events using data of source radii and seismic moments. The estimated values of the stress drops range from 1.4 to 19.2 bars. The wide range in values of the stress drops for these 16 microearthquakes with magnitudes of -1.9 to -2.6 is consistent with the stress drop variability found by Fehler and Phillips (1991) with a different approach. We suggest that the large stress drop variability reflects the stress field heterogeneity in the vicinity of a hydraulic fracture zone and this stress heterogeneity extends down to

Table 2: Source Parameters of 16 Main Microearthquakes

Event ID	Mag. Mc	Mo dyn-cm	t1/2 ms	T ms	r m	σ bars
2727	-2.0	4.6e15	2.4	5.0	8.0	3.9
2732	-2.5	1.9e15	1.0	2.2	3.5	19.2
2774	-2.2	3.2e15	1.8	4.2	6.4	5.4
2880	-2.6	1.6e15	1.2	2.8	4.3	8.7
2940	-2.3	2.7e15	1.0	3.0	4.2	15.8
2967	-2.2	3.2e15	1.6	4.0	6.1	6.2
2994	-2.5	1.9e15	1.2	2.6	4.1	14.3
3023	-2.0	4.6e15	2.2	4.6	7.4	4.9
3035	-2.4	2.2e15	1.4	2.8	4.8	8.9
3041	-2.2	3.2e15	2.2	6.4	9.0	1.9
3095	-2.2	3.2e15	1.4	3.0	4.9	11.9
3130	-2.3	2.7e15	1.4	2.8	4.8	10.6
3166	-2.1	3.8e15	1.4	2.6	4.6	17.2
3280	-1.9	5.4e15	2.2	4.8	7.6	5.4
3600	-1.9	5.4e15	3.4	7.6	12.0	1.4
3722	-2.3	2.7e15	2.0	5.6	8.0	2.3

the scale of a few meters.

Rupture Directivity and Fault Plane

Figure 12 shows the vertical seismograms of event 2967 (M=-2.2) and its EGF counterpart (event 2880, M=-2.6) recorded at three stations EE1, GT1 and PC1. Distances from the hypocenters to the stations range from 470 to 3370 meters. The epicentral separation between the two events is only 1.6 meters and the depth difference is 6 meters. The ratios between the source separation and hypocentral distances are from 0.18% to 1.2%. The two events must share an almost identical propagation path. We can see the waveform similarity in the three pairs of seismograms in Figure 12. The top frame of Figure 13 shows the RSTF of event 2697 estimated with S waves recorded at three stations. We note that there is azimuthal variation of the RSTFs. The pulse widths and pulse amplitudes of the RSTF observed at stations EE1 and GT1 are similar, but the RSTF at station PC1 has a significantly smaller pulse amplitude and broader pulse width, suggesting that the rupture propagates toward the northwest, away from station PC1.

In Figure 14, we compare the rupture direction of a single event with the growth direction of the hydraulic fracturing zone derived by Li and Cheng (1995). The rupture direction derived from source rupture directivity is consistent with the growth direction derived from seismicity temporal-spatial variation, indicating that the single event

source ruptures towards the northwest direction along a near vertical fault plane. Kaieda (1984), House *et al.* (1985) and Fehler *et al.* (1987) have discussed the fault plane solutions obtained from the larger microearthquakes accompanying the hydraulic injection recorded by both borehole geophones and seismometers of a nine-station-network on the surface. These focal mechanism studies have found that, although many different types of fault plane solutions occur, there are two that dominate (Figure 15). Furthermore, Fehler *et al.* (1987) determined which nodal plane is the real fault plane (dashed lines in Figure 15) using a three-point method. The seismicity distribution of the cluster in Figure 14 and the rupture direction derived by analyzing azimuthal variations of the RSTF of event 2967 from this study suggest the focal mechanism of the event is similar to one of the two common fault plane solutions (Figure 15, left). Results from our rupture directivity analysis confirms that the rupture indeed occurred on the near-vertical fault plane selected by Fehler *et al.* (1987) as a real fault plane.

CONCLUSIONS

It has been demonstrated that the deconvolution of empirical Green's functions can be successfully applied to extract the RSTFs for small microearthquakes induced by hydraulic fracturing. Although most of the induced microearthquakes are simple events, a few appear to be multiple events with a complex rupture process. We found source complexity for events with magnitudes of about -2. For seismic events with seismic moments of 1.6×10^15 to 5.4×10^15 dyn-cm, the source durations range from 2.2 to 7.6 s, corresponding to the fault radii of 3.5 to 12 meters. Stress drops estimated for 16 main events within the hydraulic fracture zone vary from 1.4 to 19.2 bars, suggesting that the stress-filled heterogeneity exists in the vicinity of the hydraulic fracture zone, and that it extends down to a scale of meters. We estimate the rupture direction by analyzing azimuthal variations of the RSTF of event 2967. The rupture is towards the northwest and the direction is similar to the growth direction of the hydraulic fracture zone. Our estimate of the rupture direction is compatible with the fault plane determined by a three point method (Fehler *et al.,* 1987). The range of stress drop estimates from this study is also consistent with that derived by Fehler and Phillips (1991) using an inversion method of simultaneously inverting for Q and for source parameters, indicating that the Q model they derived is a reasonable model which can correct the media attenuation effects and lead to a reliable estimate of the source parameter.

ACKNOWLEDGMENTS

We thank Drs. Scott Phillips and Mike Fehler for providing the seismic waveform data and other information. This research was supported by the Borehole Acoustics and Logging Consortium at ERL and by DOE Contract DE-FG02-86ER13636.

REFERENCES

Ammon, C.J., A.A. Velasco, and T. Lay, 1993, Rapid estimation of rupture directivity: Application to the 1992 Landers (Ms=7.4) and Cape Mendocino (Ms=7.2) California earthquakes, *Geophys. Res. Lett., 20,* 97–100.

Boatwright, J.A., 1980, A spectral theory for circular seismic sources: Simple estimates of source dimension, dynamic stress drops and radiation energy, *Bull. Seism. Soc. Am., 70,* 1–28.

Brune, J.N., 1970, Tectonic stress and the spectra of seismic shear wave from earthquakes, *J. Geophys. Res., 75,* 4997–5009.

Burger, R.W. and C.A. Langston, 1985, Source mechanism of the May 18, 1980 Mount St. Helens eruption from regional surface waves, *J. Geophys. Res., 90,* 7653–7664.

Chen, Y.T., J.Y. Zhou, and J.C. Ni, 1991, Inversion of near-source broadband accelerograms for the earthquakes source-time function, *Tectonophysics, 197,* 89–98.

Fehler, M., L. House and H. Kaieda, 1987, Determining planes along which earthquakes occur: Method and application to earthquakes accompanying hydraulic fracturing, *J. Geophys. Res., 92,* 9407–9414.

Fehler, M. and W.S. Phillips, 1991, Simultaneous inversion for Q and source parameters of microearthquakes accompanying hydraulic fracturing in granitic rock, *Bull. Seism. Soc. Am., 81,* 553–575.

Frankel, A., J. Fletcher, F. Vernon, L. Harr, J. Berger, T. Hanks, and J. Brune, 1986, Rupture characteristics and tomographic source imaging of ML 3 earthquakes near Anza, south California, *J. Geophys. Res., 91,* 12633–12650.

Fukao, Y. and M. Kikuchi, 1987, Source retrieval from mantle earthquakes by iterative deconvolution of long-period P-waves, *Tectonophysics, 144,* 249–269.

Geller, R.J. and C.S. Meuller, 1980, Four similar earthquakes in central California, *Geophys. Res. Lett., 7,* 821–824.

Hartzell, S., 1978, Earthquake aftershocks as Green's functions, *Geophys. Res. Lett., 5,* 1–4.

Hartzell, S., 1889, Comparison of seismic waveform inversion results with rupture history of a finite fault: Application to the 1986 North Palm Springs, California, *J. Geophys. Res., 94,* 7515–7534.

House, L., 1987, Locating microearthquakes induced by hydraulic fracturing in crystalline rock, *Geophys. Res. Lett., 14,* 919–921.

House, L., H. Keppler, and H. Kaieda, 1985, Seismic study of a massive hydraulic fracturing experiment, *Trans. Geotherm. Res. Counc., 9, Part II,* 105–110.

Hutchings, L. and F. Wu, 1990, Empirical Green's functions from small earthquakes: A waveform study of locally recorded aftershocks of the 1971 San Fernando earthquake, *J. Geophys. Res., 95,* 1187–1214.

Kaieda, H., 1984, Hypocenter distribution and fault plane solutions of microearthquakes induced by hydraulic fracturing as determined by observations from a surface network, *EOS Trans. AGU, 65,* 1011.

Kanamori, H., H-K., Thio, D. Dreger, E. Hauksson, and T. Heaton, 1992, Initial investigation of the Landers California earthquake of 28 June 1992 using TERRAscope, *Geophys. Res. Lett., 19,* 2267–2270.

Lay, T., J. Ritsema. C. Ammon, and T. Wallace, 1994, Rapid source mechanism analysis of the April 29, 1993 Cataract Creek (Mw =5.3), North Arizona earthquake, *Bull. Seism. Soc. Am., 84,* 451–457.

Li, Y. and C.H. Clifford, 1988, Source properties of two microearthquakes in Kilauea volcano, Hawaii, *Bull. Seism. Soc. Am., 78,* 1123–1132.

Li, Y. and M.N. Toksöz, 1993, Study of the source process of the 1992 Colombia Ms=7.3 earthquakes with the empirical Green's function method, *Geophys. Res. Lett., 20,* 1087–1090.

Li, Y., W. Rodi, and M.N. Toksöz, 1994, Seismic source characterization with empirical Green's function and relative location techniques, in *Proceedings of the 16th Annual PL/DARPA Seismic Research Symposium, Phillips Laboratory, Hanscom,* pp. 231–237.

Li, Y. and C.H. Cheng, 1995, Imaging geometry and growth rate of a hydraulic fracture zone by locating induced microearthquakes *Annual Report,* Borehole Acoustics and Logging Consortium, MIT, Cambridge, Massachusetts, this issue.

Li, Y., C. Doll, and M.N. Toksöz, 1995a, Source characterization and fault plane determinations for Mblg= 1.2 to 4.4 earthquakes in the Charlevoix seismic zone, Quebec, Canada, submitted to *Bull. Seism. Soc. Am.*

Li, Y., M.N. Toksöz, and W. Rodi, 1995b, Source time functions of nuclear explosions and earthquakes in central Asia determined using empirical Green's functions, *J. Geophys. Res., 100,* 559–674.

Li, Y., C. Doll, and M.N. Toksöz, 1995c, Derivation of source time functions and associated source parameters using EGF method for the September 1994 eastern Maine and October 1994 Central Massachusetts earthquake swarms, *Seismol. Res. Lett., 66,* 55.

Mori, J. and A. Frankel, 1990, Source parameters for small events associated with the 1986 North Palm Springs California earthquake determined using empirical Green's functions, *Bull. Seism. Soc. Am., 80,* 278–295.

Mueller, C., 1985, Source pulse enhancement by deconvolution of an empirical Green's function, *Geophys. Res. Lett., 12,* 33–36.

Pearson, C, 1982, Parameters and a magnitude moment relationship from small earthquakes observed during hydraulic fracturing experiments in crystalline rocks, *Geophys. Res. Lett., 9,* 404–407.

Velasco, A., C. Ammon, and T. Lay, 1994, Recent large earthquakes near Cape Mendocino and in the Gorda plate: Broadband source time functions, fault orientations and rupture complexities, *J. Geophys. Res., 99,* 711–728.

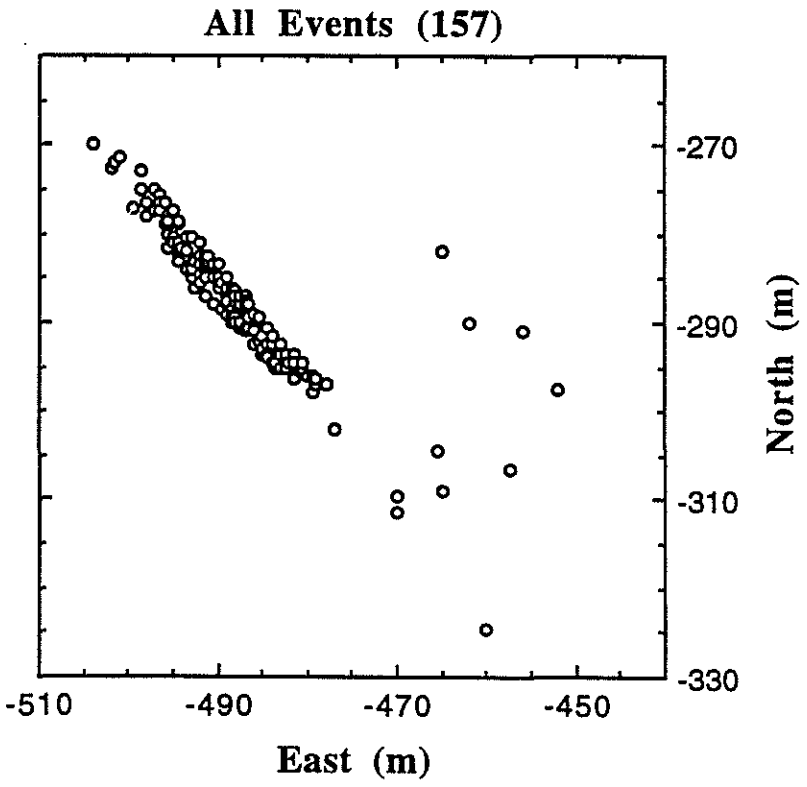

Figure 1: Map view showing epicenters of 157 microearthquakes induced by hydraulic fracturing during the HDR experiment 2032 on December 7, 1983, at Fenton Hill, New Mexico. The majority of the events delineates a hydraulic fracture zone with an azimuth of $N40°W$.

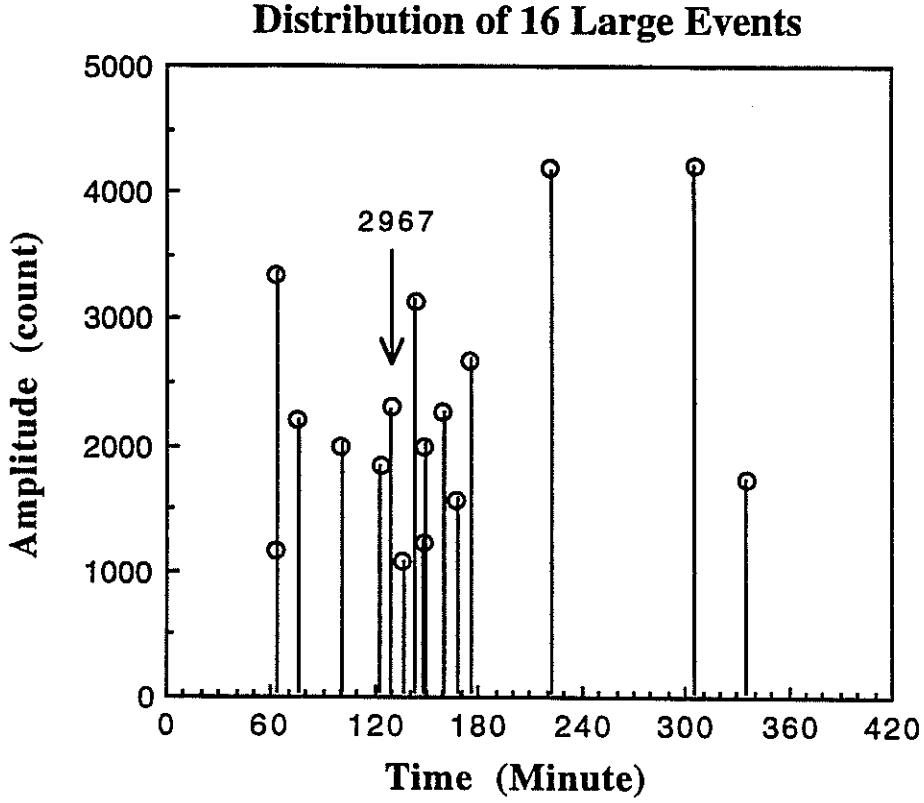

Figure 2: Temporal distribution of 16 main events shown in Table 1.

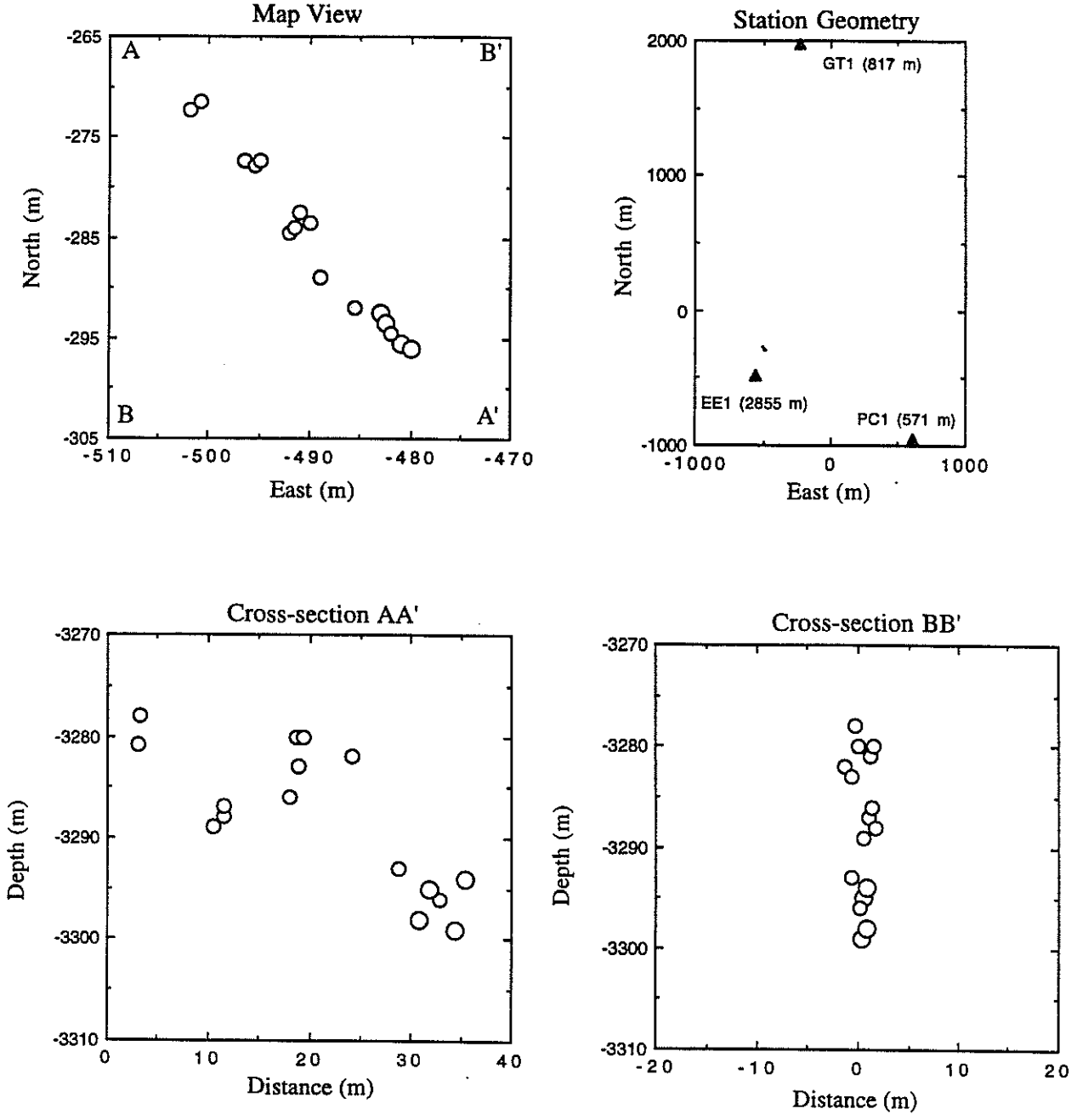

Figure 3: Map view and two vertical cross-sections showing spatial distribution of the 16 main events. Three stations used in analysis are also shown with triangles.

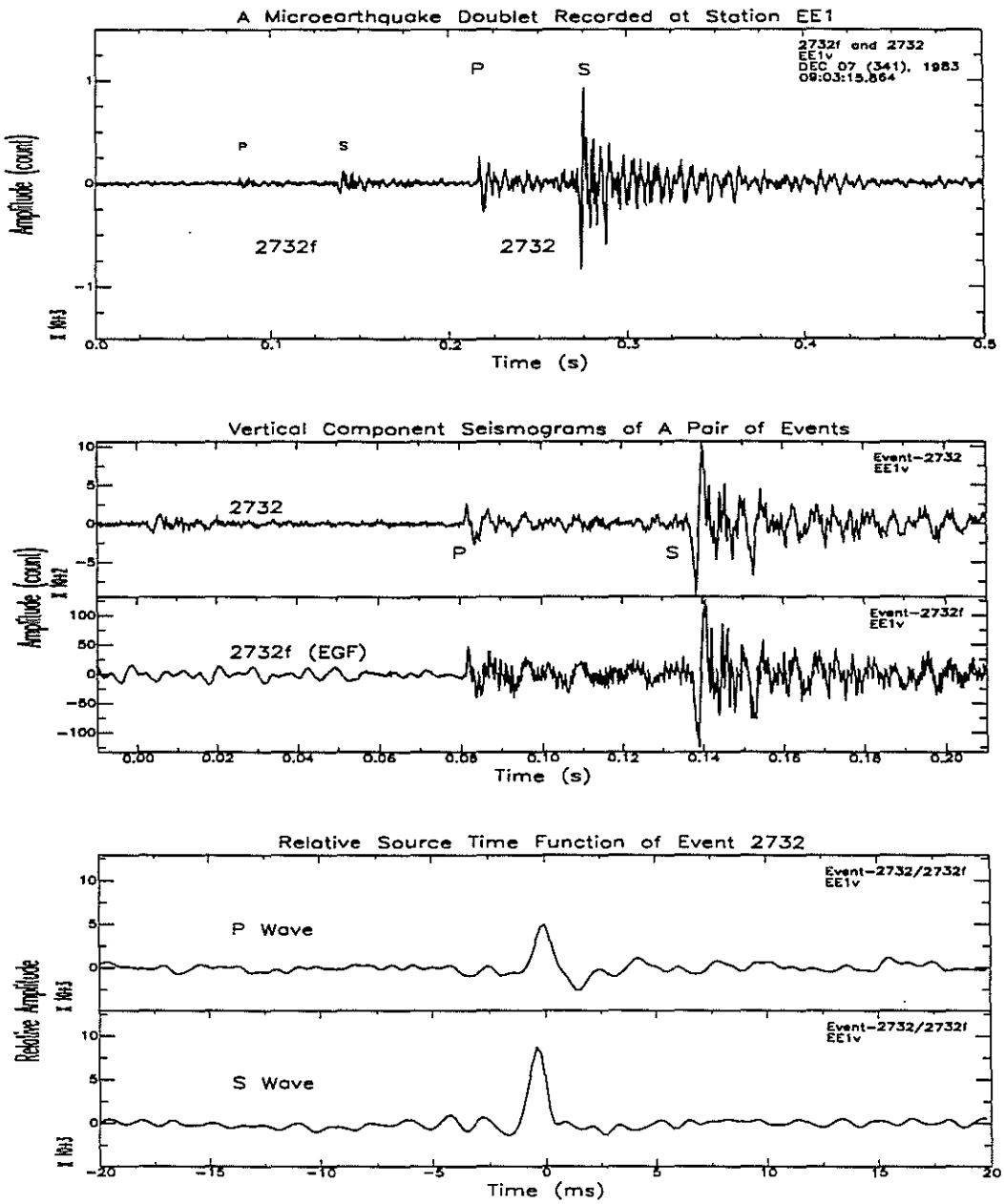

Figure 4: Example showing the procedure of retrieving RSTF using a seismic doublet and the EGF method.

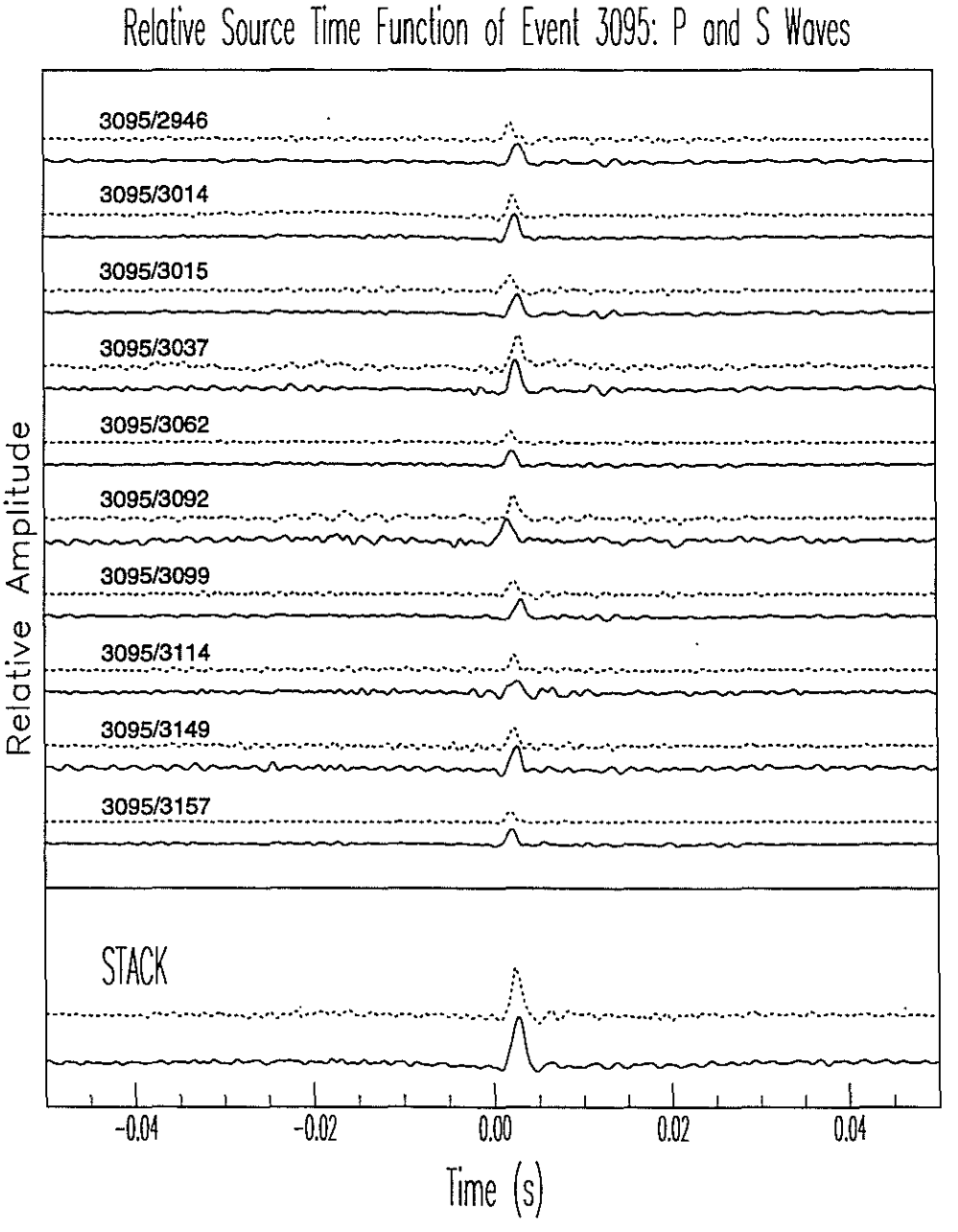

Figure 5: Relative source time function of event 3095 (M=−2.2) retrieved using both P (dashed lines) and S (solid lines) waves of 10 different EGF events recorded at station EE1. The bottom traces are stacking results for P and S waves, respectively. The RSTF indicates that this is a simple event.

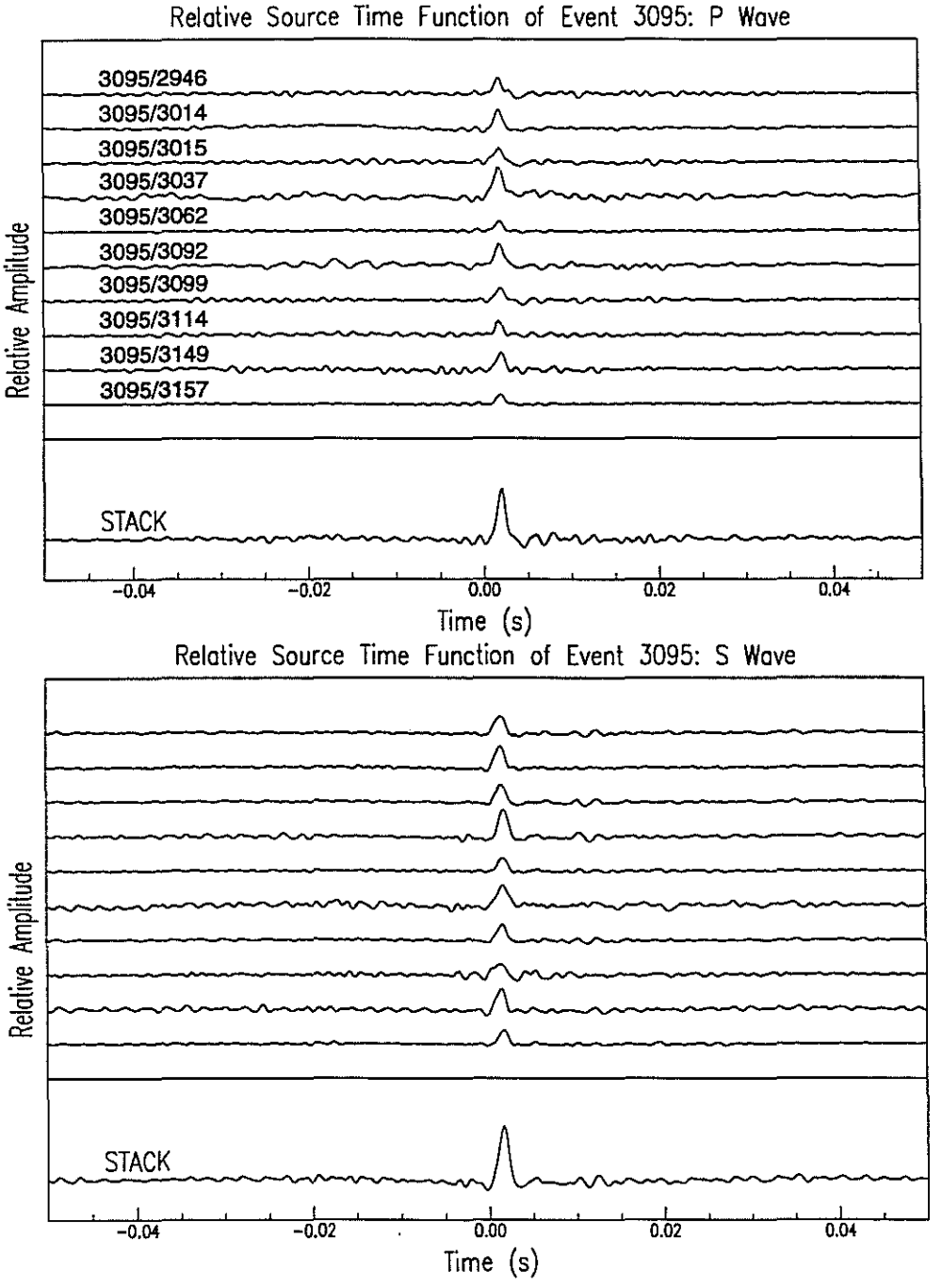

Figure 6: Top frame: RSTF of event 3095 extracted with P waves and a stacking trace. Bottom frame: RSTF of event 3095 extracted with S waves and a stacking trace. The RSTF retrieved with S waves is better than that with P waves.

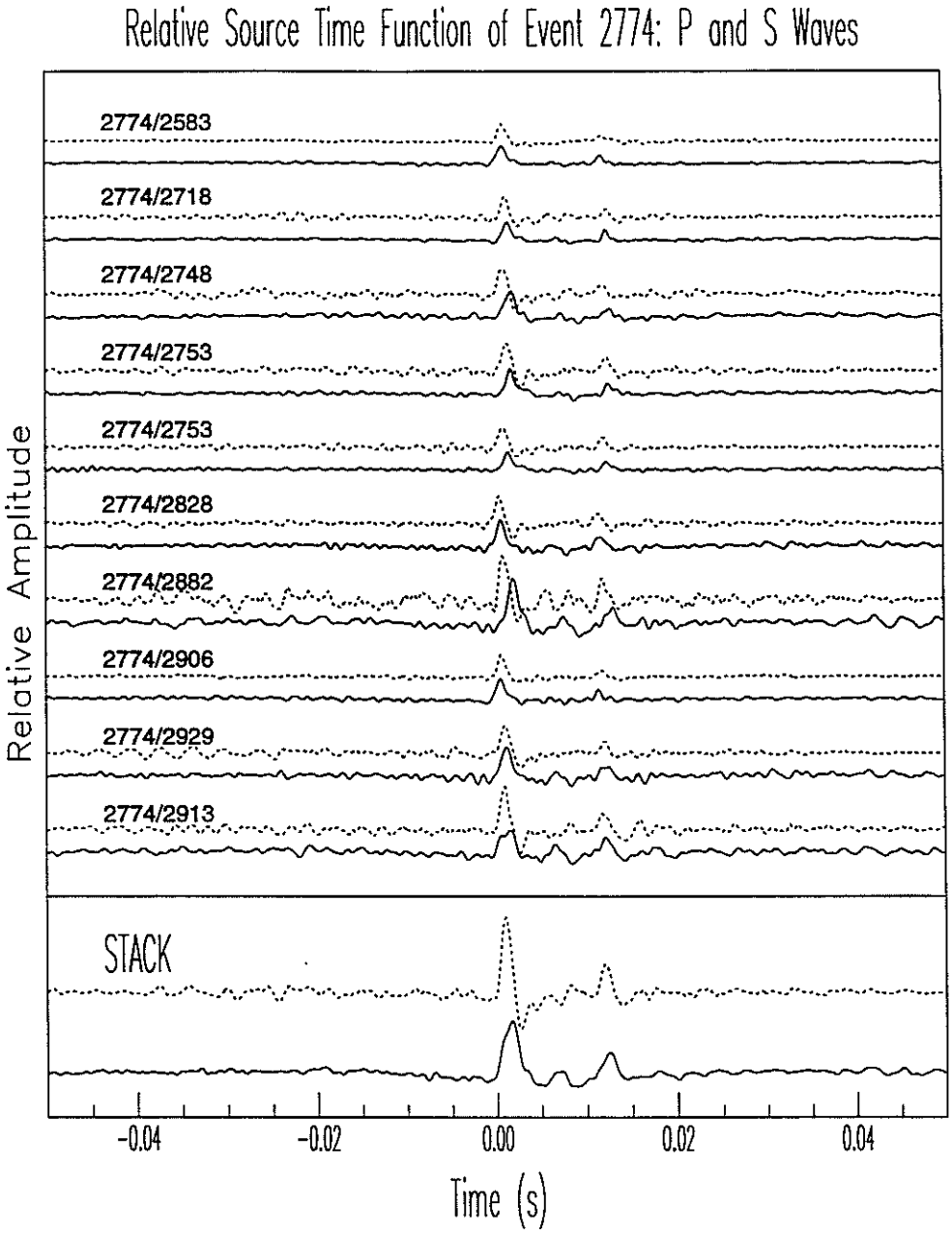

Figure 7: Relative source time function of event 2774 (M=−2.2) retrieved using both P (dashed lines) and S (solid lines) waves of 10 different EGF events recorded at station EE1. The bottom traces are stacking results for P and S waves, respectively. The RSTF shows that event 2774 is a complex event.

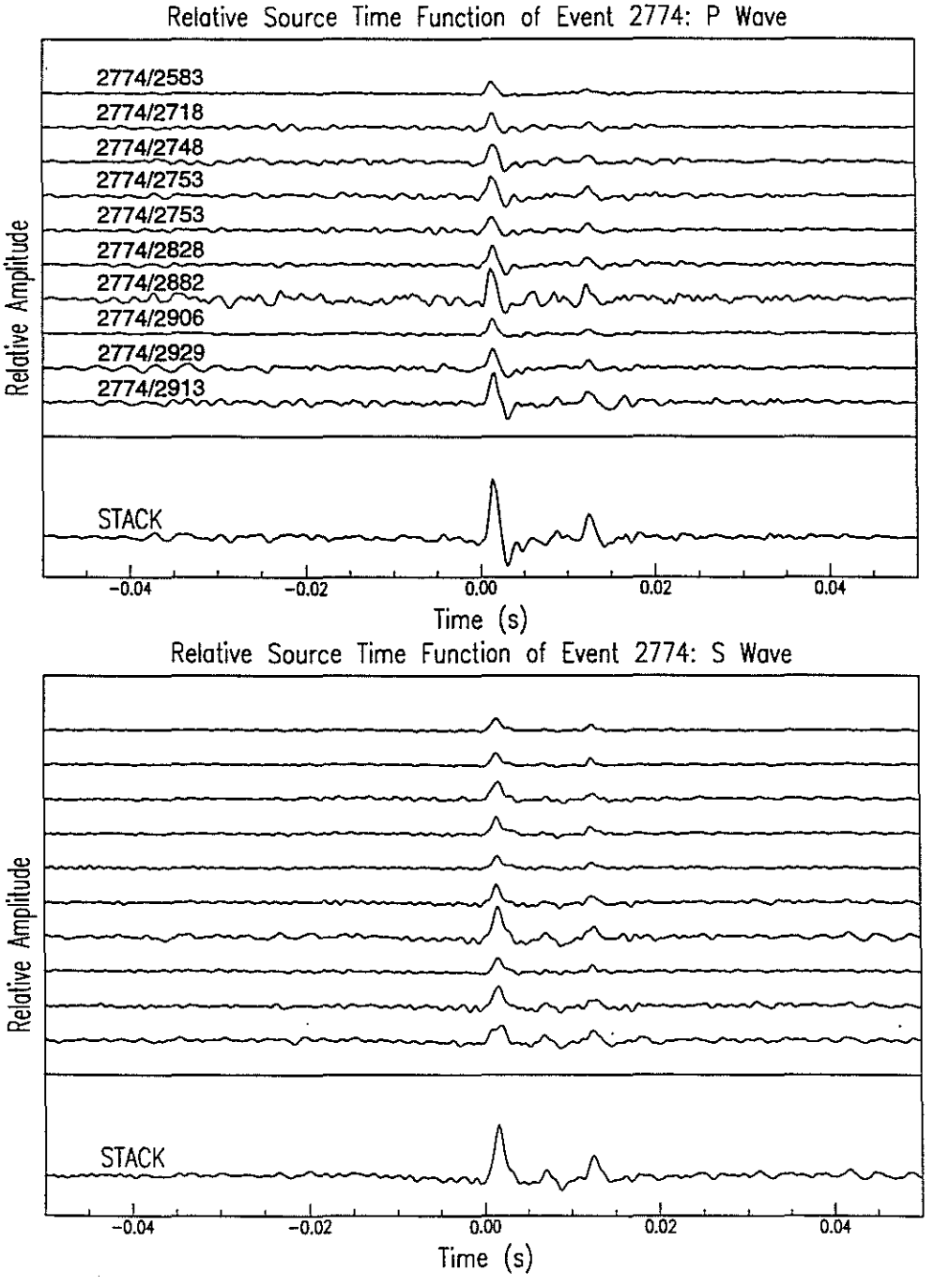

Figure 8: Top frame: RSTFs of event 2774 extracted with P waves and a stacking trace. Bottom frame: RSTFs of event 2774 extracted with S waves and a stacking trace. The RSTF retrieved with S waves is better than that with P waves.

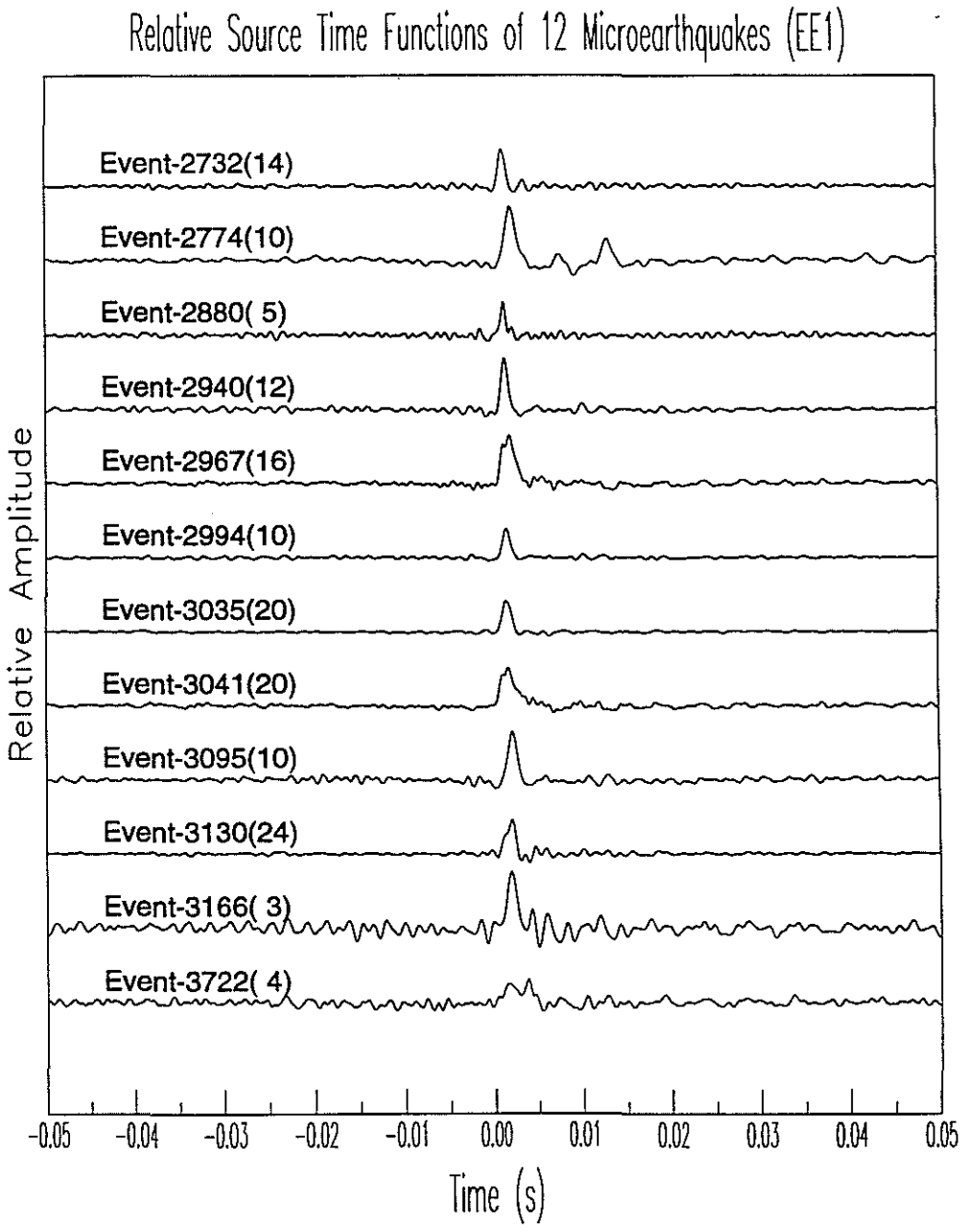

Figure 9: RSTFs of 12 main events (M=−2.6 to −2.1) retrieved with S waves recorded at station EE1.

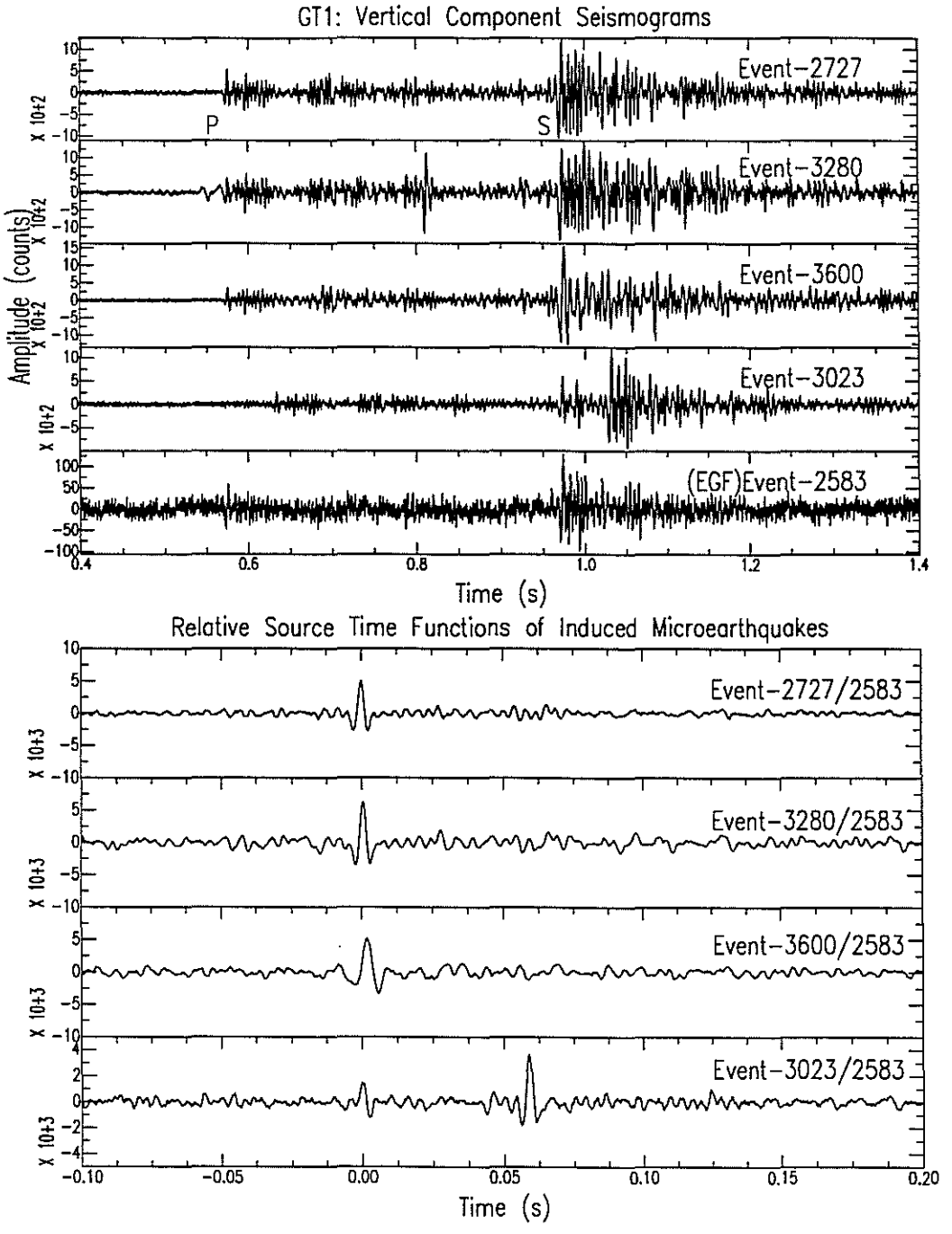

Figure 10: Top frame: Vertical component seismograms for the four largest induced earthquakes (M = −1.9 to −2.0) under study and the waveform of an EGF event (2853). Bottom: RSTFs retrieved for the largest induced microearthquakes. Three of them are simple pulses, but event 3023 appears to be a complex event.

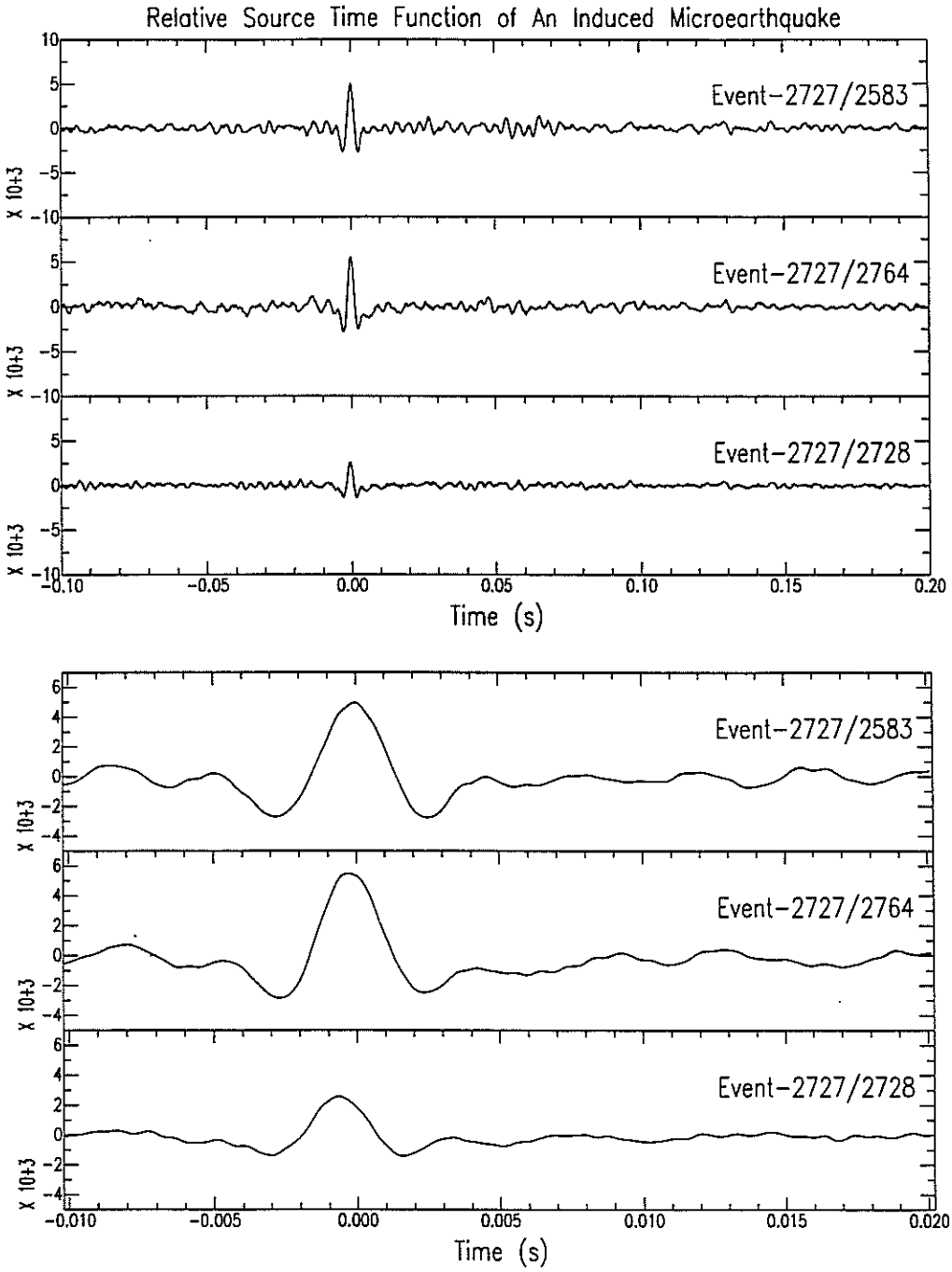

Figure 11: Top frame: RSTFS of event 2727 retrieved with three different EGF events. The enlarged seismograms allow us to obtain a better measurement of the source duration.

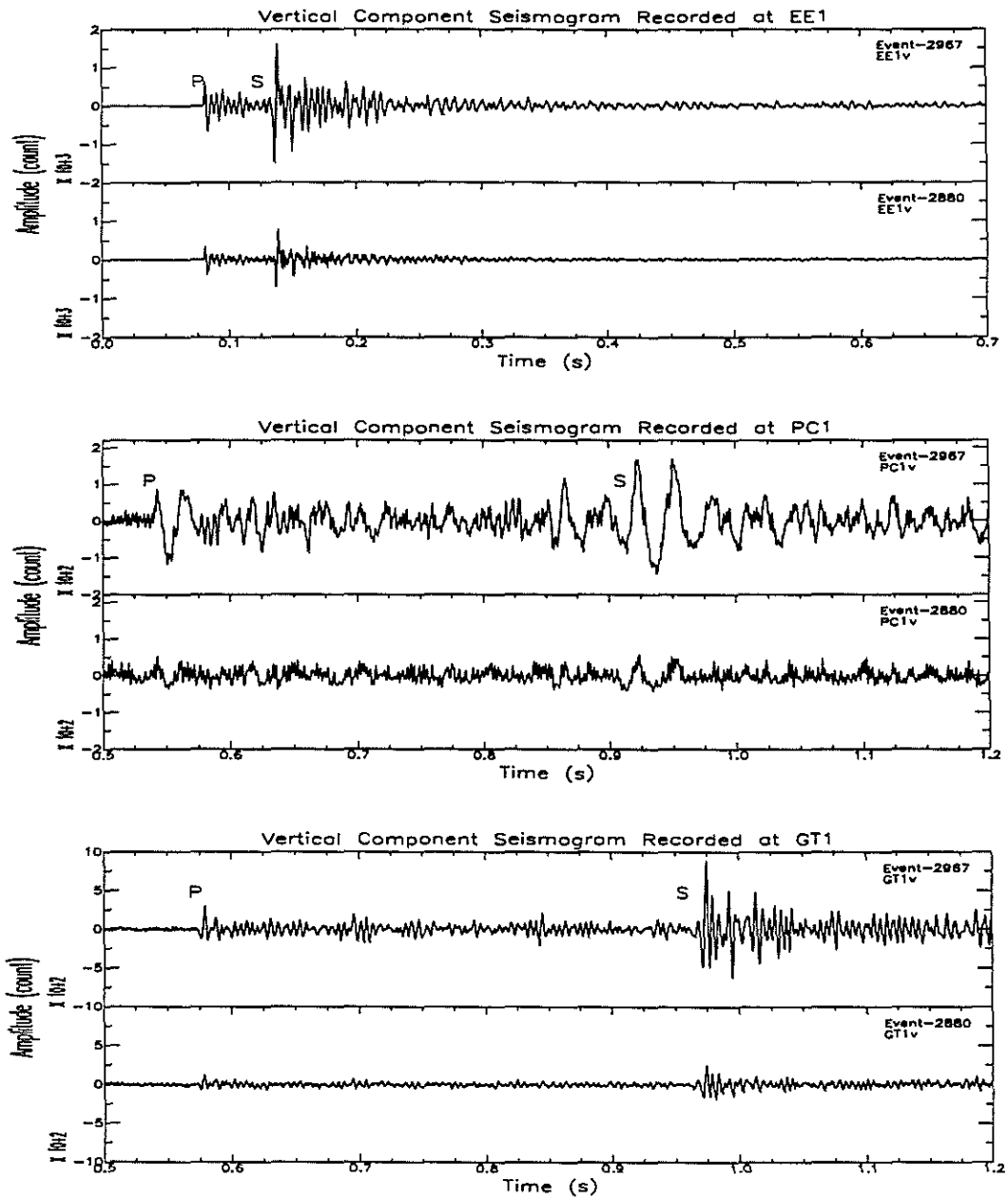

Figure 12: Seismograms of events 2967 and 2880 recorded at three stations. The S waves of the smaller event (2880) were used as the EGF to retrieve the RSTF for the larger event 2967.

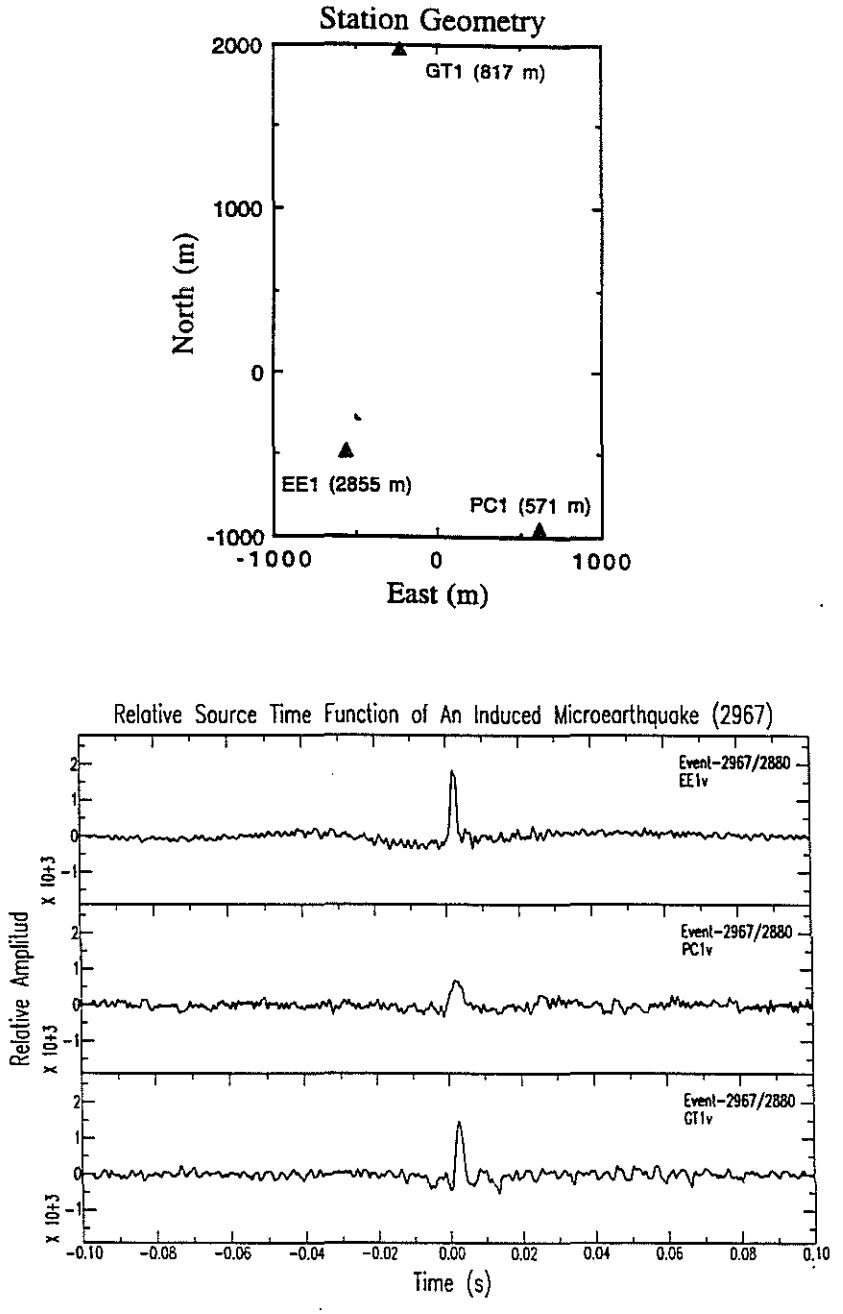

Figure 13: Top frame: Relative source time function of event 2967 retrieved from S waves recorded at three stations. Note the azimuthal variation of pulse widths and amplitudes. Bottom frame: The azimuthal variation of the RSTFs indicates the source of 2967 rupture propagates northwest, away from station PC1.

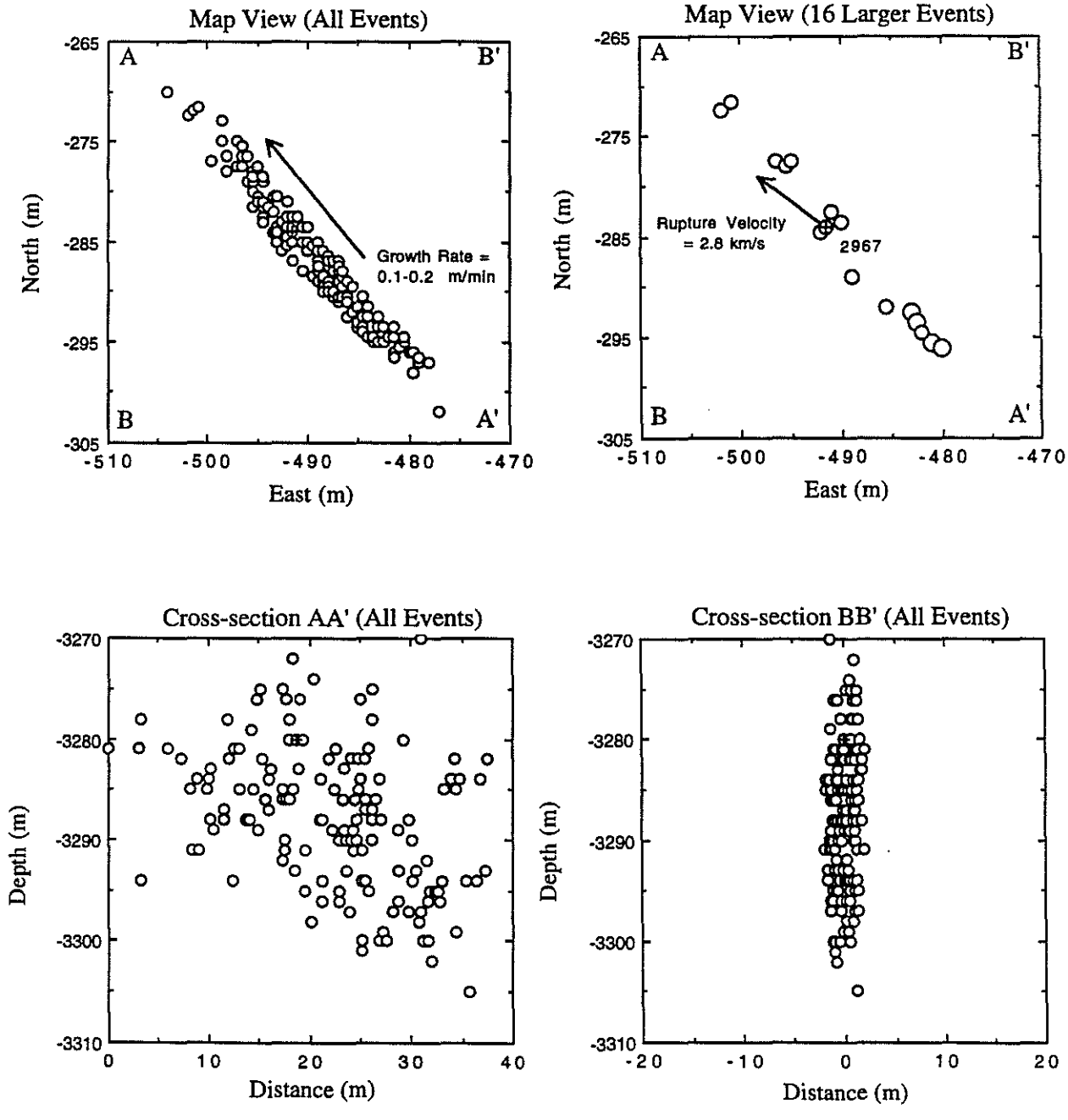

Figure 14: Comparison of the growth direction of the hydraulic fracture zone and the rupture direction of a single seismic event.

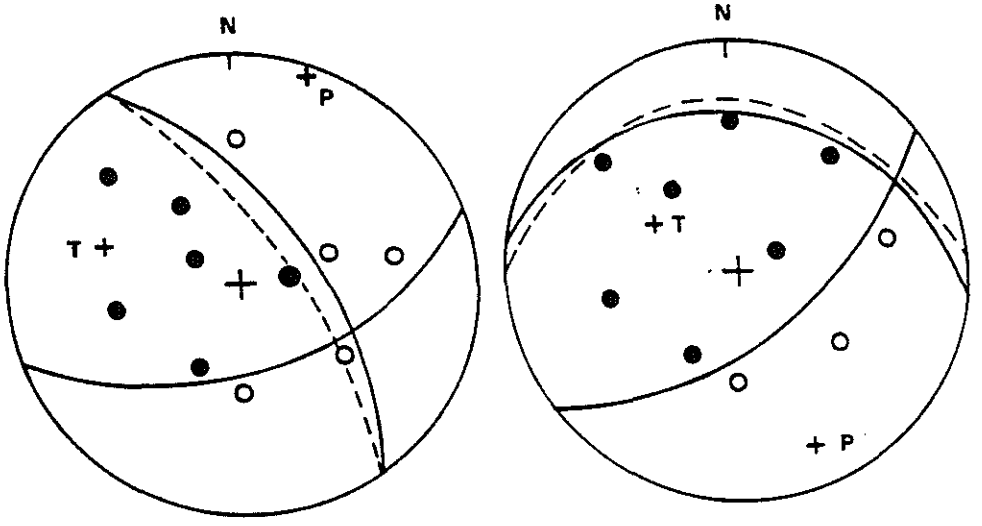

Figure 15: Two most common fault plane solutions form the hydraulic injection (from Fehler *et al.*, 1987). The focal mechanism of event 2967 may be very similar to the one on the left in Figure 15. Our rupture directivity analysis for event 2967 prefers that the rupture of the event is on a vertical fault plane along a northwest direction.